On the feedback from super stellar clusters. I. The structure of giant HII regions and HII galaxies

Guillermo Tenorio-Tagle

Instituto Nacional de Astrofísica Optica y Electrónica, AP 51, 72000 Puebla, México; gtt@inaoep.mx

Casiana Muñoz-Tuñón

Instituto de Astrofísica de Canarias, E 38200 La Laguna, Tenerife, Spain; cmt@ll.iac.es

Enrique Pérez

Instituto de Astrofísica de Andalucía (CSIC), Camino bajo de Huetor 50, E 18080 Granada, Spain; eperez@iaa.es

Sergiy Silich

Instituto Nacional de Astrofísica Optica y Electrónica, AP 51, 72000 Puebla, México; silich@inaoep.mx

Eduardo Telles

Observatório Nacional, Rua José Cristino 77, 20921-400, Rio de Janeiro, Brazil; etelles@on.br

ABSTRACT

We review the structural properties of giant extragalactic HII regions and HII galaxies based on two dimensional hydrodynamic calculations, and propose an evolutionary sequence that accounts for their observed detailed structure. The model assumes a massive and young stellar cluster surrounded by a large collection of clouds. These are thus exposed to the most important star-formation feedback mechanisms: photoionization and the cluster wind. The models show how the two feedback mechanisms compete with each other in the disruption of clouds and lead to two different hydrodynamic solutions: The storage of clouds into a long lasting ragged shell that inhibits the expansion of the thermalized wind, and the steady filtering of the shocked wind gas through channels carved within the cloud stratum. Both solutions are here claimed to be concurrently at work in giant HII regions and HII galaxies, causing their detailed inner structure.

This includes multiple large-scale shells, filled with an X-ray emitting gas, that evolve to finally merge with each other, giving the appearance of shells within shells. The models also show how the inner filamentary structure of the giant superbubbles is largely enhanced with matter ablated from clouds and how cloud ablation proceeds within the original cloud stratum. The calculations point at the initial contrast density between the cloud and the intercloud media as the factor that defines which of the two feedback mechanisms becomes dominant throughout the evolution. Animated version of the models presented can be found at http://www.iaa.csic.es/~eperez/ssc/ssc.html.

1. Introduction

Multiple studies during the last decades have addressed the impact of photoionization, stellar winds and supernova explosions on interstellar matter (ISM). Disruptive events that re-structure the birth place of massive stars and their surroundings, while leading to multiple phase transitions in the ISM (see e.g. Comeron 1997; Yorke et al. 1989; García-Segura et al. 2004; Hosokawa & Inutsuka 2005 and Tenorio-Tagle & Bodenheimer 1988 and references therein). On the other hand, giant molecular clouds, the sites of ongoing star formation, present a hierarchy of clumps and filaments of different scales whose volume filling factor varies between 10% to 0.1% (see McLow & Klessen, 2004, and references therein). As the efficiency of star formation in molecular clouds is estimated to be $\leq$ 10% (Larson 1988; Franco et al. 1994) the implication is that the bulk of the cloud structure remains after a star forming episode. All of these studies are relevant within the fields of interstellar matter and star formation and, in particular, regarding the physics of feedback, a major ingredient in the evolution of galaxies and thus in cosmology.

From the observations, we know that the energetics of major bursts of star formation allow us to track galaxies up to very high redshifts, however, by the time these sources are found star formation is already in a well advanced stage of its evolution, and thus we do not know for certain, not even for the closest sources, which is the state of the matter left over from a major massive burst of star formation. We do know that giant extragalactic HII regions and HII galaxies are excellent examples of the impact of massive stars on the ISM. They belong to the same class of objects because they are powered by young massive bursts of star formation. Also because of their similar physical size, morphology and inner structure. Detailed studies of 30 Doradus (see Chu & Kennicutt 1994; Melnick et al. 1999), NGC 604 (Sabalisck et al. 1995; Yang et al 1996) and several giant extragalactic HII regions and HII galaxies (Muñoz-Tuñón et al. 1996; Telles et al. 2001; Maíz-Apellániz

et al. 1999) have been designed with the aim of unveiling the inner structure and dynamics of the nearest examples. All of them present a collection of nested shells that enclose an X-ray emmiting gas and that may extend up to kpc scales. Some of the largest shells have stalled while others present expansion speeds of up to several tens of km s^{-1}. Detailed HST images have also confirmed these issues for HII galaxies as well (Martin et al. 2002; http://hubblesite.org/newscenter/newsdesk/archive/releases/2004/35/image/a). All of these sources, as in the studies of Telles et al (2001) and Cairós et al. (2001), present a central bright condensation coincident with the massive burst of stellar formation. In giant HII regions and in some HII galaxies (cf. Figure 10) this is resolved as the brightest filament or a broken ragged shell sitting very close to the exciting cluster. The central bright condensations are much smaller than the sizes of the ionized volumes, which become more and more diluted at large radii to finally merge with the background galactic interstellar medium.

The energy powering these giant volumes comes from the recently found unit of massive star formation: super star clusters (Ho 1997; see also Lamers et al. 2004 and references therein). Massive concentrations of young stars within the range of 10^5 $M_\odot$ to several 10^6 $M_\odot$, all within a small volume $\sim 3 - 10$ pc. Multiple young super star clusters are found within the most luminous HII galaxies and starburst galaxies, as in M82 where a collection of two hundred of them have been found within the central 150 pc of the dwarf galaxy (Melo et al. 2005), while the most compact HII galaxies and particularly giant HII regions, are structured by the action of only one or a few of these exciting clusters.

However, despite multiple efforts we still lack a detailed model. None of the numerical simulations in the literature, that have considered either the powerful winds or the impact of the ionizing radiation on the surrounding ISM, or both, have reproduced the kpc-scale morphology and inner structure of giant HII regions and HII galaxies. There are thus a number of central questions that remain in this field. And thus apart from the fact that we ignore the initial condition, the distribution of matter around new massive bursts of star formation, it is crucial to understand how the central brightest condensations or ragged shells survive or withstand the full power of the exciting clusters, and how the multiple nested shells develop within the large-scale ionized volume and acquire their inner filamentary structure.

Here we address all these issues by means of two dimensional (2-D) hydrodynamics. As in all other studies, our initial conditions are arbitrary and perhaps much more so in this case, as we have surrounded the central powerful SSC by a large concentration of spherical, static, cloudlets, reflecting perhaps the simple fact that we do not know the initial distribution of interstellar matter around a new major burst(s) of star formation. Our initial and boundary conditions are also arbitrary, in the sense that we approach the energetics from stellar clusters following the frequently used mode of instantaneous star formation (see Leitherer & Heckman

1995), although a continuous star formation spread over a few Myr may be a more reasonable approximation. In section 2 we give a detailed description of the boundary and initial conditions used in our calculations. Section 3 describes the results of four different cases in which we explore the impact that energetic winds or photoionization, or both, may have on the selected cloudlet distribution and its surrounding gas. Our conclusions together with a full discussion of the results are given in section 4.

2. Feedback from massive star clusters

Superstellar clusters are now recognized as the main unit of massive star formation in starburst galaxies (Ho 1997), and their mechanical energy and radiative output the main feedback restructuring agents of the ISM (see Tenorio-Tagle et al. 2005). Here we assume, in all cases, a major central star formation burst with a stellar mass M_{SC} ($= 3 \times 10^6$ M$_\odot$) and a Salpeter IMF for stars between 1 and 100 M$_\odot$, all concentrated within a radius R_{SC} = 5 pc.

2.1. The initial condition

The mechanical energy and the UV photon output from the massive stellar cluster is here confronted with an ISM structured into a collection of clouds. Three dimensional calculations are required if the clouds are spherical, however, in this first 2-D approach to the problem each 3-D individual cloud is instead a torus of which a 2-D cross-sectional cut is a disk, as depicted in Figure 1. Just as in other recent contributions (e.g. Pittard et al. 2005), to reduce the computational cost we restrict ourselves to 2-D simulations. Although we do expect some differences between 2-D and 3-D calculations, clearly an important insight on the evolution and on the role played by the various parameters can still be obtained from the less computationally demanding 2-D simulations. Several two dimensional calculations using as initial condition the adiabatic SSC model of Chevalier & Clegg (1985) have been performed with the explicit Eulerian finite difference code described by Tenorio-Tagle & Muñoz-Tuñón (1997, 1998). This has been adapted to allow for the continuous replenishment of matter within the SSC volume (see below). The time dependent calculations do not consider thermal conductivity but do account for radiative cooling (Raymond et al. 1976) for a gas with solar metallicity. Several calculations were made to reassure that the spatial resolution used led to a convergent solution. All calculations here presented were made with the same numerical

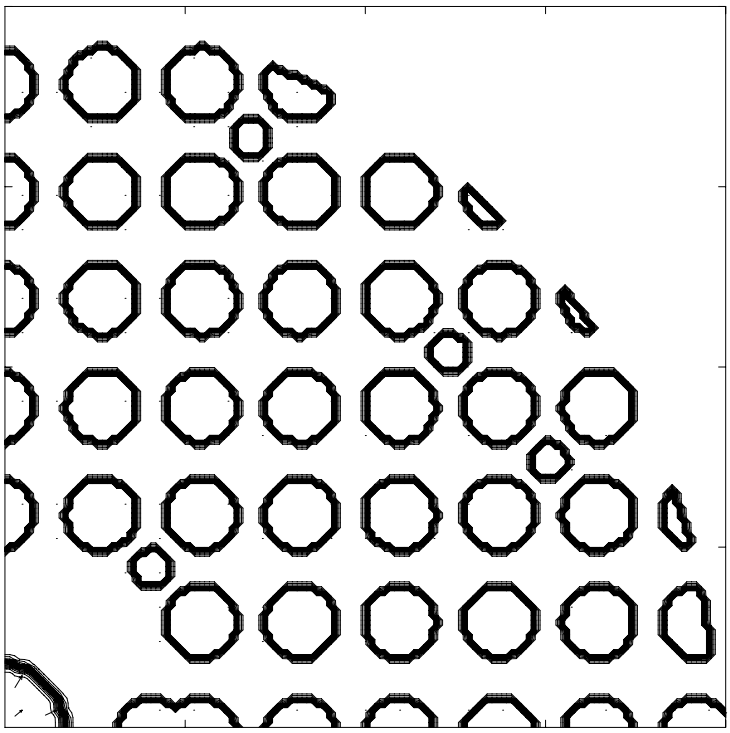

Fig. 1.— The initial condition. The panel shows a cross-sectional cut along the computational grid showing isodensity contours with a separation $\Delta \log \rho = 0.18$. The central superstar cluster has a power of 10^{41} erg s^{-1} and a radius of 5 pc. Note that the velocity field within the central SSC grows from the sound speed value to its terminal velocity $V_\infty = 10^3$ km s^{-1}, here represented by the largest arrows. The plot displays one quadrant of the full cloudlet distribution within the central 50 pc $\times$ 50 pc of the total computational grid which spans 200 pc $\times$ 200 pc.

resolution of $\Delta R = \Delta Z = 0.33$ pc and all of them with an open boundary condition along the grid outer edge.

Here we assume that most of the gas left over from star formation conforms a large collection of dense cloudlets around a central, massive ($M_{SC} = 3 \times 10^6$ M$_\odot$) starburst (see Figure 1). In the various cases here shown the only difference is the cloudlet gas density ($n_c = 10^2$ and 10^3 cm^{-3}). The dense cloudlets are embedded and initially in pressure equilibrium with a low density medium ($n_{ic} = 0.1$ cm^{-3}) that permeates the whole computational grid (200 × 200 pc). In all cases the stationary clouds with a size, $r_{cl} = 7.7 \times 10^{18}$ cm, have been placed at arbitrary locations (see Figure 1), with an almost constant separation $\Delta R = 2 \times 10^{19}$ cm, $\Delta Z = 2.2 \times 10^{19}$ cm, except for the first two rows near the grid equator for which the separation $\Delta Z = 2.4 \times 10^{19}$ cm. There are also a few smaller clouds scattered within the cloud stratum placed there, as all other clouds, with the sole aim of obstructing the general radial outflow expected in an otherwise constant density case.

2.2. Boundary conditions

In all cases we have assumed that within the region that encompasses the recently formed stellar cluster (R_{SC}), the matter ejected by strong stellar winds and supernova explosions is fully thermalized (Chevalier & Clegg 1985; see also Raga et al. 2001; Silich et al. 2004). This generates the large overpressure responsible for the mechanical luminosity associated to the cluster which results from the mechanical energy (L_{SC}) and mass ($\dot{M}_{SC}$) deposition rates, within the star forming region. The total mass and energy deposition rates define the central temperature T$_{SC}$ ($\sim 1.5 \times 10^7$ K) and thus the sound speed c_{SC} (~ 500 km s^{-1}) at the cluster surface.

$$T_{SC} = \frac{0.3\mu}{k} \frac{L_{SC}}{\dot{M}_{SC}}, \tag{1}$$

where μ is the mean mass per particle and k the Boltzmann constant. On the other hand, the density of matter streaming from the SSC surface (ρ_{SC}) can be obtained from the stationary condition in which the matter exiting the cluster surface (R_{SC}) per unit time, has to be equal to the mass deposition rate ($\dot{M}_{SC}$):

$$\dot{M}_{SC} = 4\pi R_{SC}^2 \rho_{SC} c_{SC}. \tag{2}$$

The outflow starts its expansion with its sound speed (c_{SC}), however, as it streams away it is immediately accelerated by the steep pressure gradient to rapidly reach its terminal velocity

($V_\infty \sim 2c_{SC} \sim 10^3$ km s^{-1}). This is due to a fast conversion of thermal energy into kinetic energy of the resultant wind. Throughout the calculations, the density, temperature and thus sound speed, are replenished within R_{SC} at every time step. In this way, as the wind develops, its density, temperature and thermal pressure approach their asymptotic values: $\sim r^{-2}$, $r^{-4/3}$ and $r^{-10/3}$, respectively, while, the wind velocity reaches its maximum value (V_∞).

2.3. The time evolution

Cases A and B consider the impact that each of the feedback agents, capable of structuring the ISM (SSC winds and photoionization), may have independently on the selected cloudlet distribution. In both cases the cloudlet gas number density is $n_c = 10^3$ cm^{-3}. The results shown in Figure 2 correspond to case A, that considers only a powerful SSC wind ($L_{SC} = 10^{41}$ erg s^{-1}). Figure 3 displays the other extreme situation (case B) in which only photoionization has been considered. Figure 2 shows density and temperature along a time sequence and the four panels in Figure 3 display only the run of density of the photoionized material (all at $T \sim 10^4$ K) at selected evolutionary times. The color coded figures indicate steep gradients both in density and in temperature, tracing strong compression and surfaces across which large heating/cooling occurs and thus indicate the location of shocks. Also noticeable in the plots are the sudden changes in velocity and direction of the various streams and thus the velocity field is also a good tracer of the presence of shock waves.

2.4. Case A- The wind-cloud stratum interaction

The powerful isotropic wind from the central SSC immediately develops a leading shock moving with a velocity V_S. As this begins to interact with the surrounding gas and as the free wind approaches the cloud stratum a global reverse shock is established (see Figure 2). At the reverse shock the wind is thermalized, although initially as the shape of the reverse shock follows closely the density or cloudlet stratification it acquires a multiple bow configuration. Consequently, large azimuthal sections of the isotropic wind are only partly thermalized and redirected by the bow sections of the reverse shock to stream around the encountered cloudlets (see the time sequence shown in Figure 2). The wind-cloudlet interaction leads to a complicated hydrodynamical set of events as it also drives a transmitted shock into the obstacle cloudlets. The strength of this shock is proportional to the square root of the contrast density between the two media ($V_t = V_S(\rho_{ic}/\rho_c)^{1/2}$). Given the density contrast between clouds and the intercloud medium these disturbances move slowly into the

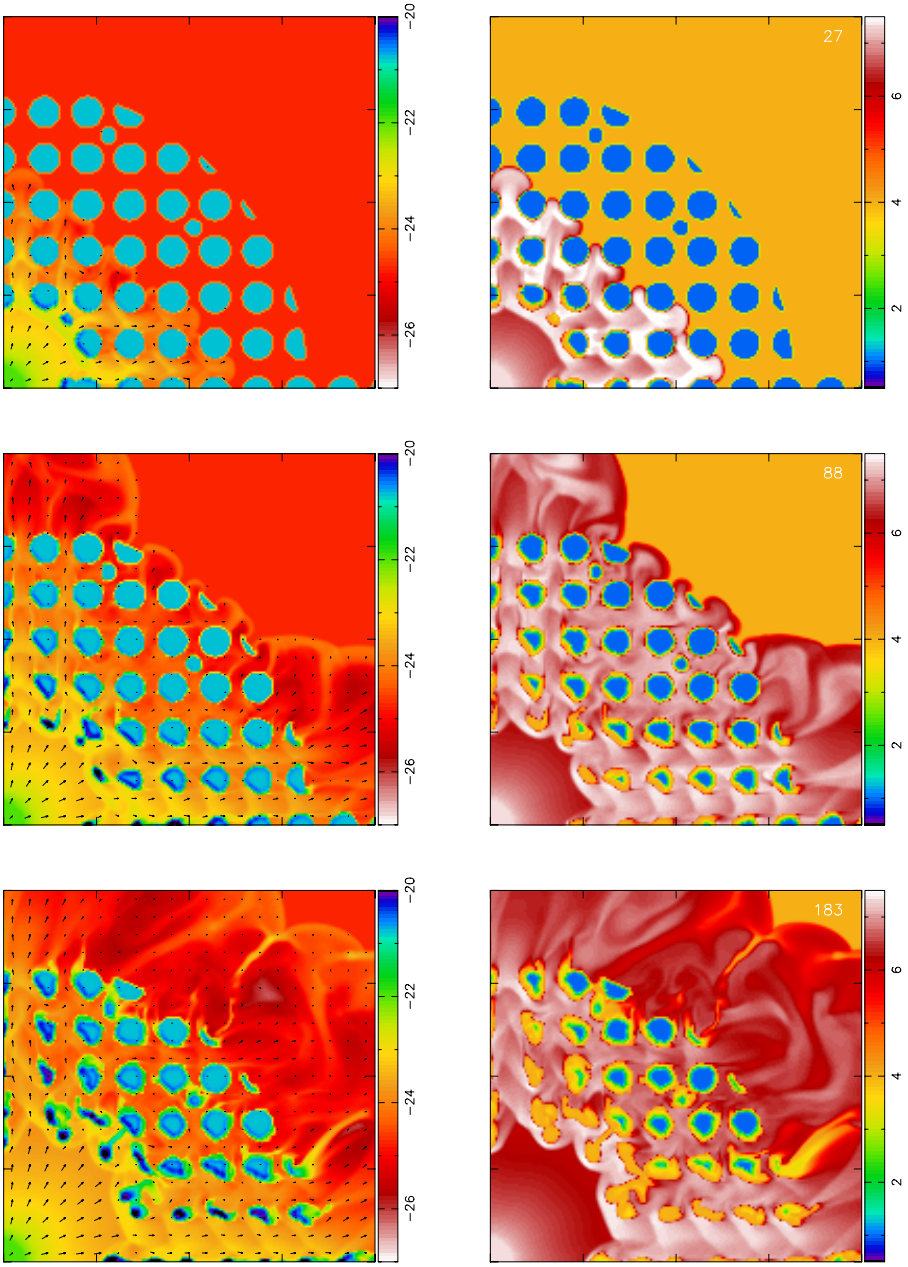

Fig. 2.— Case A. The initial interaction of the SSC wind with the cloud stratum. The panels display cross-sectional cuts along a section of the computational grid showing: isodensity (left panels, in log units of g cm^{-3}) and temperature (right-hand side panels, in log units of K). The velocity field is also plotted in the density panels where the longest arrow represents 10^3 km s^{-1}. The model is shown at three different times: 2.7 $\times 10^4$ yr, 8.8 $\times 10^4$ yr and 1.83 $\times$ 10^5 yr, respectively. The size of the panels is 60 pc by 60 pc.

clouds and in this way, the main shock, rushing at first with its velocity V_S, rapidly circumvents the condensations while leaving a large pressure behind them. This pressure induces also secondary shocks into the overtaken cloudlets, what reduces their physical cross-section. However, the strength of the secondary shocks is also bound by the cloud-intercloud contrast density and, as in the case of the transmitted shocks, secondary shocks evolve also slowly into the clouds. The main shock and its overtaken matter, both driven by the partly thermalized wind, soon encounter other cloudlets and this induces, once again, the whole hydro response (reverse bow-shock into the wind and transmitted and secondary disturbances into the cloudlets).

The partly thermalized wind behind the multiple bow shocks, plays an important role in the erosion of cloudlets (Tenorio-Tagle & Rozyczka 1986; Klein et al. 1994). This is through Kelvin-Helmholtz surface instabilities promoted by the rapid streams of shocked wind gas, that continuously peel the outer skins of clouds (see density and temperature in the second and third panels of Figure 2). During the process, the matter ablated from the clouds is driven into elongated streams, shaped by the multiple currents of thermalized wind gas, while forming bridges into neighbouring clouds.

Clearly, as a result of all of these multiple interactions the wind is finally fully thermalized and then streams to follow the leading shock into all possible paths of least resistance in between the cold ($T \sim 10$ K) clouds. Eventually, say after 8.8 $\times 10^4$ yr, the shocked wind and its leading shock finally begin to emerge at several places into the surrounding low density medium. The further evolution, also shown in Figure 2 (third row), displays the multiple channels taken by the shocked wind through the cloud stratum as well as all of those that eventually become blocked by matter ablated from clouds near the SSC. At the same time, clouds at the outer edge of the cloudlet distribution become ablated and conform large, almost radial streams of gas with a temperature $T \leq 10^4$ K embedded into the hotter $T > 10^7$ K shocked wind gas (see last row of panels in Figure 2).

2.5. Case B- Photoionization effects

The effects induced by photoionization act in a completely different manner. Here we assumed in all cases a large UV photon flux, able to establish a large-scale HII region with a size (a Strömgren radius) much larger than the size of the computational grid. The hydrodynamical response to photoionization alone (shown in Figure 3) is also significant and is to compete with a central wind in the disruption of the dense stratum. Upon turning the cluster on, the temperature of the initially neutral medium is almost immediately set, through photoionization, to the equilibrium temperature of the resultant HII region (T_{HII}

$\sim 10^4$ K). This causes a large pressure imbalance between the cloud and the intercloud medium which immediately promotes the expansion and dilution of the cloudlets into the low density intercloud volume, through a plethora of well localized "champagne flows" (see Tenorio-Tagle 1979). As a result of such a champagne bath, the low density paths between cloudlets are to become narrower and narrower as time goes by.

The expansion of the dense stratum driven by the UV radiation, is aimed at restoring pressure equilibrium everywhere and as all the gas presents the same temperature, $T \sim T_{HII}$, this could only be reached if the fluid acquires an even density everywhere. This promotes a significant large-scale champagne outflow that rapidly composes an expanding halo, a growing rim of ionized gas around the cloudlet distribution, that ends up acquiring a speed of the order of 40 km s^{-1} (see Figure 3). Meanwhile within the cloud stratum, the expansion of clouds leads to multiple well localized converging flows that also rapidly build new condensations between the original cloudlets. The expansion of the latter also promotes converging flows that end up restoring, at least partially, the original condensations, to then start once again their disruption.

In the absence of a central wind, the central cavity is also filled with matter evaporated from condensations originally set close to the core of the cloud stratum (see the time sequence shown in Figure 3).

2.6. Case C. Star-formation feedback into a high density cloudlet distribution

There are thus two competing events: The pressure acquired by the wind at the reverse shock ($P_{bubble} = \rho_w v_\infty^2$) defines the velocity that the leading shock may have as it propagates into the intercloud medium ($V_S = (P_{bubble}/\rho_{ic})^{0.5}$), and thus, as a first approximation, if the cloudlet distribution has an extent D_{cl} the time for the leading shock to travel across it is t_s ($= D_{cl}/V_S$). On the other hand, the pressure gradient between ionized cloudlets and the intercloud medium, established through photoionization, is to disrupt clouds and lead to a constant density medium in a time $t_d = \alpha d_{cs}/(2c_{HII})$; where $d_{cs}/2$ is half the average distance or separation between clouds, c_{HII} is the sound velocity in the ionized medium and α is a small number ($\sim$ 4 - 6) and accounts for the number of times that a rarefaction wave ought to travel (at the sound speed) the distance $d_{cs}/2$ to replenish the whole volume with an average even density $< \rho >$. In this way if the cloud disruption process promoted by photoionization leads to an average $< \rho >$ that could largely reduce the velocity of the leading shock ($V_S = (P_{bubble}/ < \rho >)^{0.5}$), then t_s could be larger than t_d, leading, as shown below, to an effective confinement of the shocked wind, at least for a significant part of the evolution.

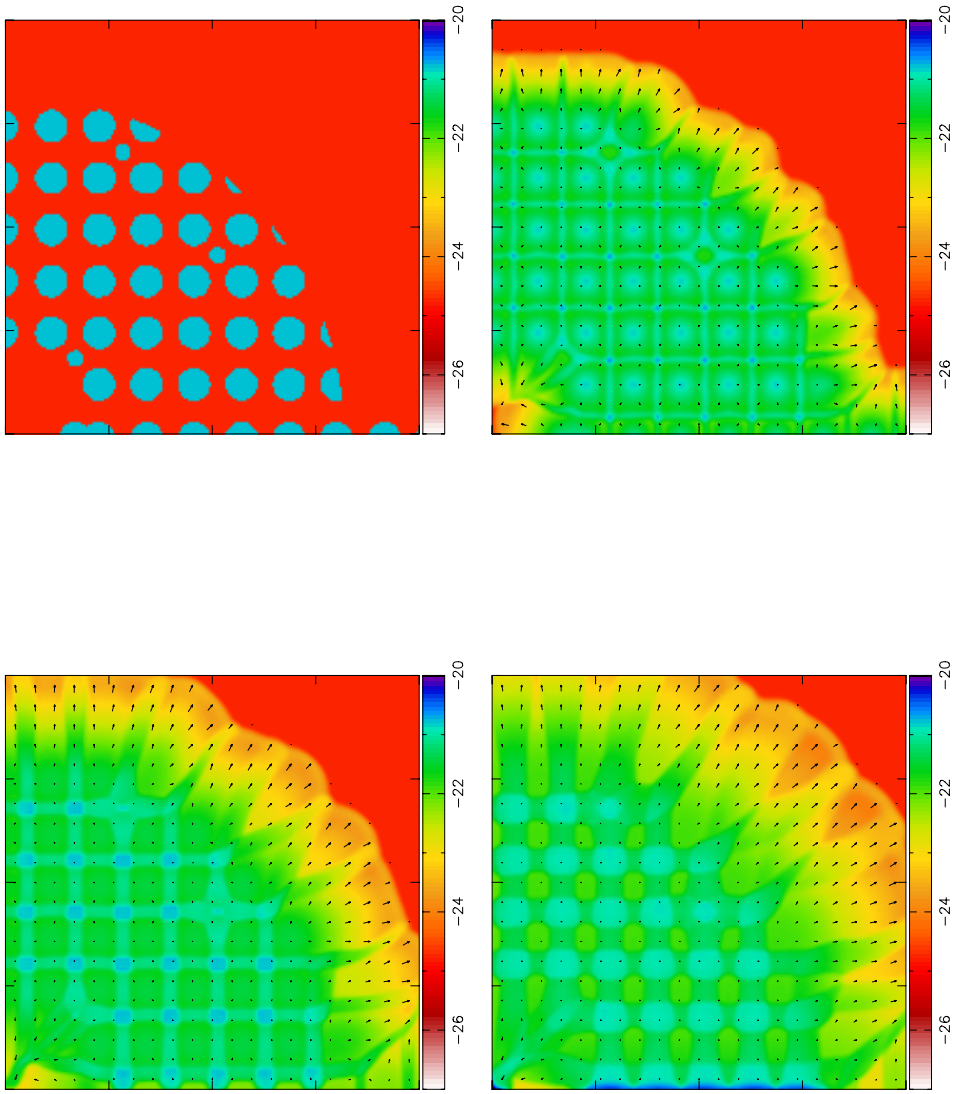

Fig. 3.— Case B. Photoionization effects. The panels show cross-sectional cuts along the computational grid showing isodensity values (in log units of g cm^{-3}) and the velocity field for which the longest arrow represents 45 km s^{-1}. The size of the panels is 60 pc × 60 pc. The evolutionary times are: The initial condition (t = 0; upper left panel) and 2.1 × 10^5 yr (upper right-hand panel), 3.3 × 10^5 yr (lower left-hand panel) and 4.6 × 10^5 yr (bottom right-hand panel), respectively.

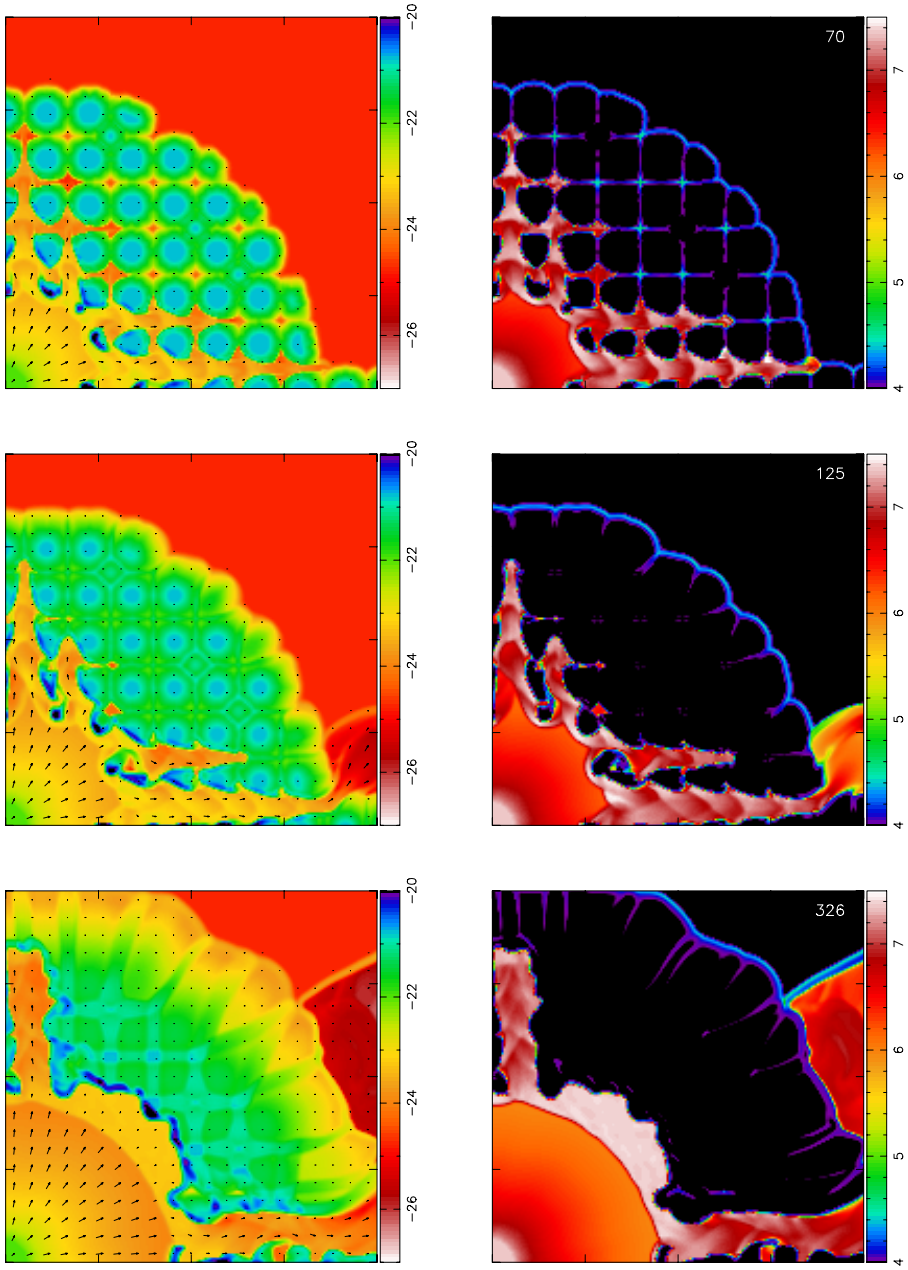

Fig. 4.— The star formation feedback into a dense cloudlet distribution. Case C, $n_c = 10^3$ cm^{-3}, $L_{SC} = 10^{41}$ erg s^{-1}. The panels display cross-sectional cuts along a section of the computational grid showing: density (left panels) and temperature (right-hand side panels) together with the velocity field for which the longest arrow represents 10^3 km s^{-1}. The evolution time (from top to bottom panels) is: 7 $\times 10^4$ yr, 1.25 $\times 10^5$ yr and 3.26 $\times$ 10^5 yr, respectively. The figure shows the 60 pc $\times$ 60 pc central section of the computational grid.

Case C considers both feedback events: a powerful SSC wind with a power of 10^{41} erg s^{-1} and a ionizing photon flux (10^{54} UV photons s^{-1}) sufficient to photoionize initially all the matter within the computational grid. Figure 4 displays the rapid evolution of the photoionized cloud stratum, filling almost everywhere the low density intercloud zones, while spreading the density of the outermost cloudlets into the surrounding intercloud medium. This causes the development of an increasingly larger ionized expanding rim around the cloudlet distribution and leads to a rapid enhancement of the intercloud density. The supersonic expansion of the champagne gas can better be traced by the multiple isothermal shocks, apparent in the temperature plots (these are depicted as narrow blue lines in the first and second temperature panels in Figure 4). Noticeable also in Figure 4, is the location and shape of the global reverse shock into the wind, that evolves from an initially ragged surface across which the isotropic wind is only partly thermalized, to an almost hemispherical surface that fully thermalizes the wind. Initially, after crossing the reverse shock the hot wind drives the leading shock into the cloudlet distribution and this immediately looks for all possible paths of least resistance in between clouds. This fact, as shown in the density and temperature panels in Figure 4, diverts the shocked wind into multiple streams behind every overtaken cloudlet, diminishing steadily its power to reach the end of the cloudlet distribution before the outermost clouds expand and block many of the possible exits into the low density background gas. Note that in the absence of clouds, the wind traveling at 10^3 km s^{-1}, would have taken $2{\times}10^5$ yr to get to the edge of the computational grid. In the calculation only one channel, the initially widest channel close to the grid equatorial axis, across which the original cloudlet spacing was set slightly larger than in the rest of the distribution, is succesfully crossed by the leading shock and the thermalized wind behind it, after $\sim 10^5$ yr of evolution (see second row of panels in Figure 4). A second channel through the cloud stratum is completed (close to the symmetry axis) after a time $t = 5 \times 10^5$ yr (see first and second rows of panels in Figure 5). All other possibilities, evident for example in the second frames of Figure 2, are here blocked by the large densities resultant from the champagne bath (compare Figure 4 with Figure 2).

Figure 5 displays details of the resultant structure after 4.6×10^5 yr of evolution. At this time, a bunch of partly shocked cloudlets and most of the extended outer rim of photoionized gas obstruct still the direct expansion of the thermalized wind into the background low density ISM. Matter able to emit at optical wavelengths is depicted in the figures at temperatures in the range $T \sim 10^4 - 10^5$ K. Within this temperature range is the low density background gas and the ablated cloudlet gas driven into an almost hemispherical elongated ragged shell trapped between the shocked wind and the extended photoionized rim. More gas at this temperature range is found at the outer boundary of the large-scale expanding shells, as well as in the initial sections of the elongated filaments that extend from the

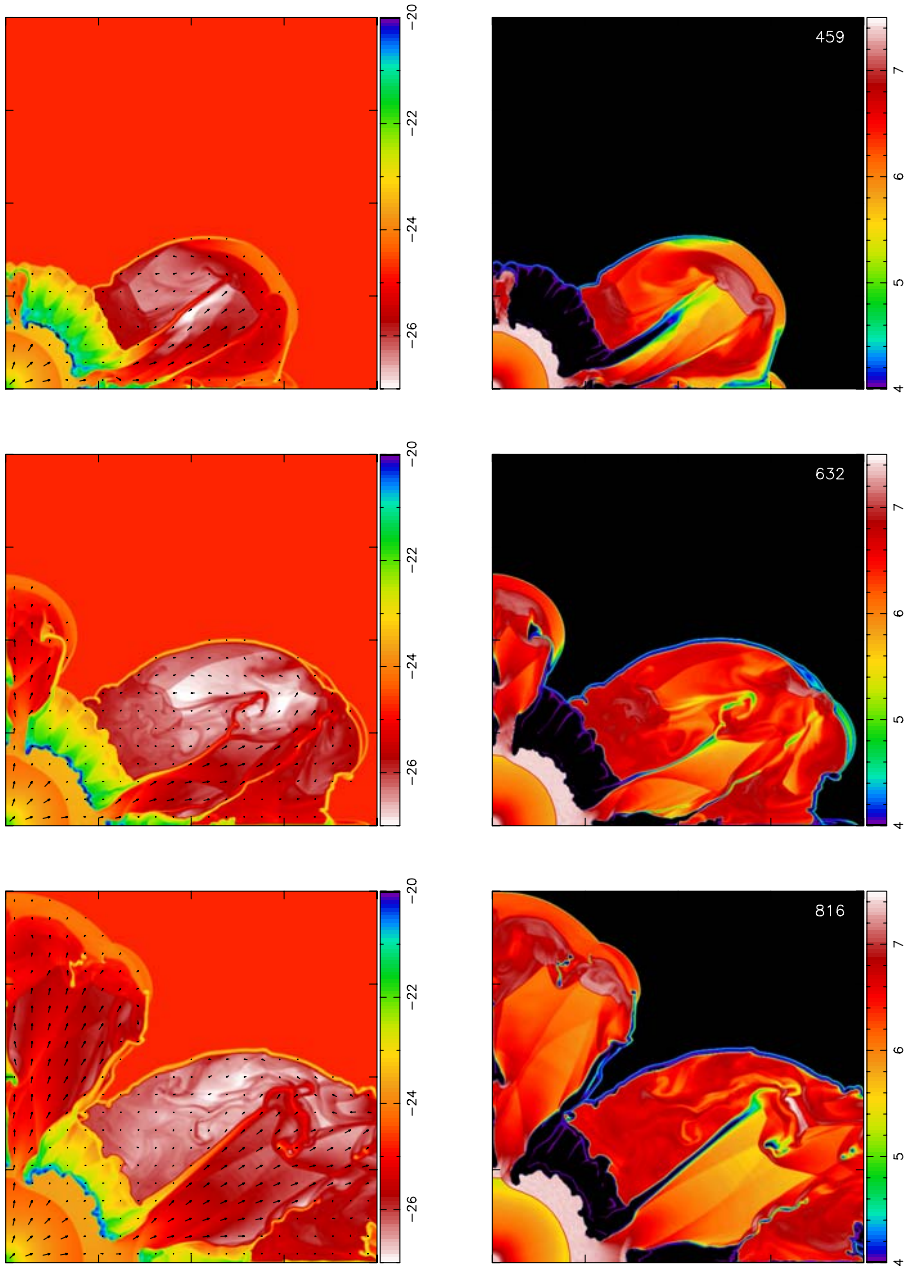

Fig. 5.— The time evolution of case C, as in Figure 4, density and temperature plotted at three different times (from top to bottom panels): 4.6 $\times 10^5$ yr, 6.32 $\times 10^5$ yr and 8.16 $\times$ 10^5 yr, respectively. The panels show the full computational grid (200 pc $\times$ 200 pc).

original cloudlet distribution well into the interior of the large-scale bubbles. The filaments result from cloud ablation, and delineate at least initially, the open channels across which the streams of thermalized wind matter exit the cloudlet distribution. The rapid streams across the open channels thus promote the build up of large-scale shells with a significant inner filamentary structure.

Figure 5 displays also the total extent, shape and evolution of the resultant filaments. Indeed, the remains of ablated cloudlets can span up to hundreds of pc away from their original location. The continuous drag imposed by the rapid shocked wind streams, shock and heat the ablated gas up to temperatures similar to those of the hot thermalized wind matter, while the ablated cloud parcels acquire the speed of the streams. As time proceeds, radiative cooling allows the thin large-scale outer shells and the filamentary inner structure to become more prominent within the temperature range $10^4 \leq T \leq 10^5$ K causing it to become more apparent at optical wavelengths, while most of the volume remains hot ($T \geq 10^6$ K) and detectable only in the X-ray regime.

Clear in all panels, with the help of the velocity field, is also the location of the global reverse shock that thermalizes the central wind. Most of the wind energy, throughout the calculation, is radiated away (see below) while the shocked wind confronts the collection of cloudlets driven to compose the dense ragged slowly moving shell that covers and blocks most of the SSC sky. The strongly decelerated hot wind gas however, meets its sonic point close to the open channels to stream supersonically and later be partly redirected by multiple oblique and crossing shocks. Only a small fraction of the SSC mechanical luminosity is channeled into the giant shells and this explains their slowness to fill the computational grid, at the same time that multiple filaments enhance the structure within the giant bubbles.

The last calculated model (at $t = 8.16 \times 10^5$ yr; third row in Figure 5) shows the moment of merging of the giant shells while these have grown to exceed the dimensions of the computational grid. At the center of the plot one can see the well developed free-wind region bound by the reverse inner shock. The shocked wind occupies now a broader zone (~ 15 pc in radial extent) and is bound by the cloud matter now composing the densest (brightest) and slowly expanding ragged shell that has just began to move into the photoionized outer rim. All of this structure is now surrounded by the large-scale merging superbubbles, at the edge of which the swept up matter collapses into multiple thin outer shells.

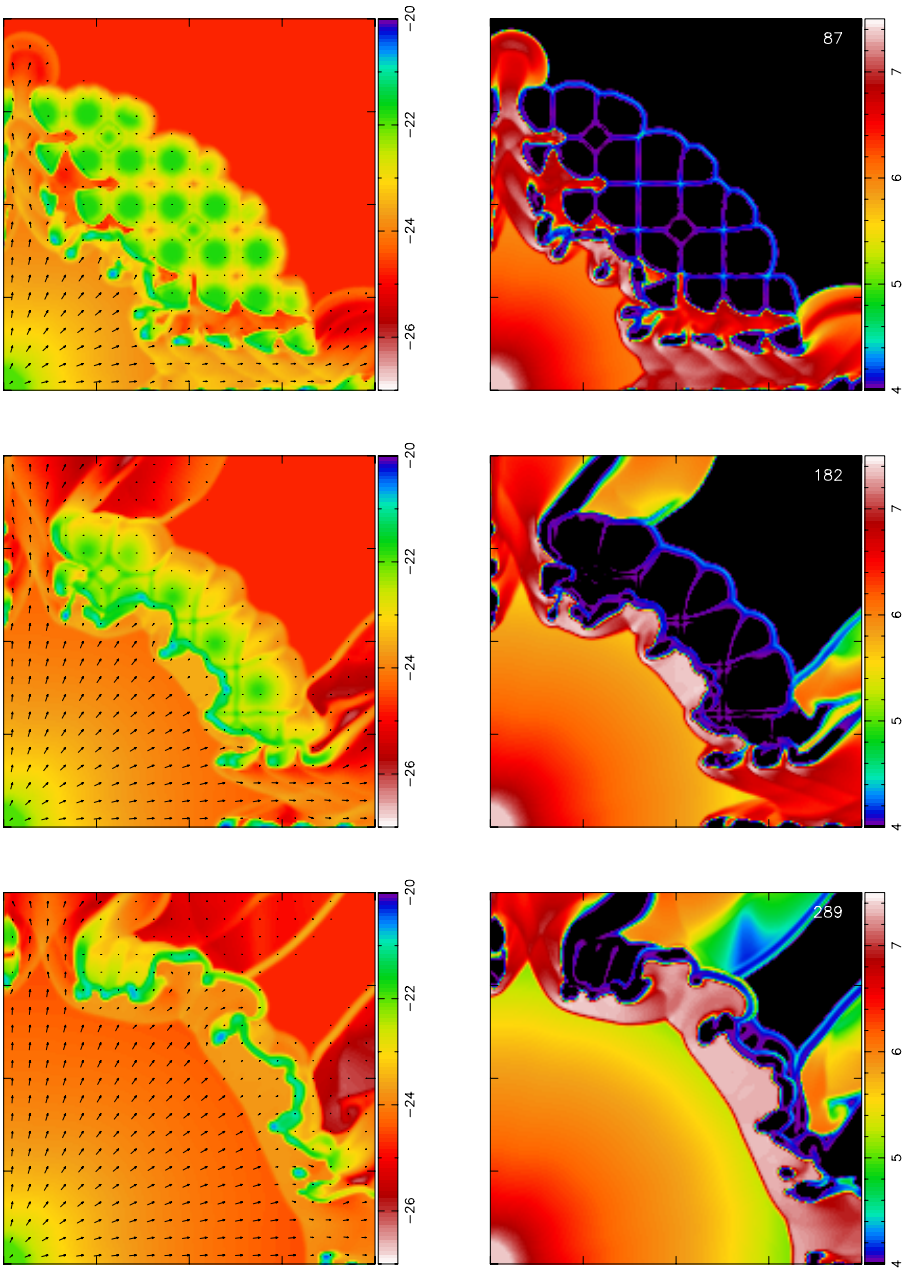

Fig. 6.— The time evolution. Case D, $n_c = 10^2$ cm^{-3}, $L_{SC} = 10^{41}$ erg s^{-1}. The same as Figure 4 at three different times: 8.7 $\times 10^4$ yr, 1.82 $\times 10^5$ yr and 2.9 $\times$ 10^5 yr, respectively. The figures shows the inner 60 $\times$ 60 pc section of the computational grid.

2.7. Case D. Star-formation feedback into a low density cloudlet distribution

Here we show the evolution that results from a low density cloudlet distribution (n_c = 100 cm $^{-3}$) being impacted by the energetics from a massive $3{\times}10^6$ $M_\odot$ cluster. The input is $L_{SC} = 10^{41}$ erg s^{-1} and 3×10^{53} ionizing photons per second. The latter causes throughout the calculation an HII region with a size larger than the computational grid. The results (in Figures 6 and 7), are to be compared with those of case C, shown in Figures 4 and 5, shown at the same physical scales. The evolution of this case reproduces all features found in case C although it proceeds much faster. Clearly, the mass evaporated from the clouds through the multiple champagne flows, enhances the density and the thermal pressure everywhere and causes, as in case C, that the cloud stratus as a whole survives much longer further downstream. However in this case, the initial contrast density between clouds and the intercloud gas is so small that it allows the wind to become dominant from the very start of the calculation. Figure 6 shows how the shocked wind rushes through the cloudlet distribution and is able to find many of the possible channels much earlier than in the case of a denser cloud stratum. It is also able to rapidly store the clouds into an elongated and ragged slowly moving shell. This, as in the former case, inhibits, at least for a significant fraction of the evolution, the direct propagation of the shocked wind into the low density background gas. However in this case, the ragged shell that contains most of the ablated clouds collected together by the action of the shocked wind, becomes unstable towards the end of the calculation (see Figure 7) as it begins to move into the extended photoionized rim that developed earlier around the original cloud stratum. The ragged shell is in this way disrupted into a collection of fragments that immediately become exposed to the rapid streams that develop as the inner reverse shock acquires once again a multiple bow shock configuration. Meanwhile, the ablation of the resultant fragments provides the large-scale superbubbles with an enhanced inner filamentary structure (see Figure 7).

2.8. Summary

As a summary of the calculation, Figure 8 shows the mass and energy budgets, as a function of time for cases C and D. The various lines in Figure 8a and c represent, from top to bottom: the total mass in the computational grid, which grows through the SSC mass deposition rate (labelled “total” in the figures). Most of the mass in the grid moves with a small velocity (< 50 km s^{-1}). This includes all the photoionized gas as well as the slowly moving cloud matter overtaken by the leading shock (marked ”slow” in the figures). The cloudlets and intercloud medium (ic) lines represent the gas with zero velocity within the grid, that preserve their original density values, both of these are largerly reduced as a

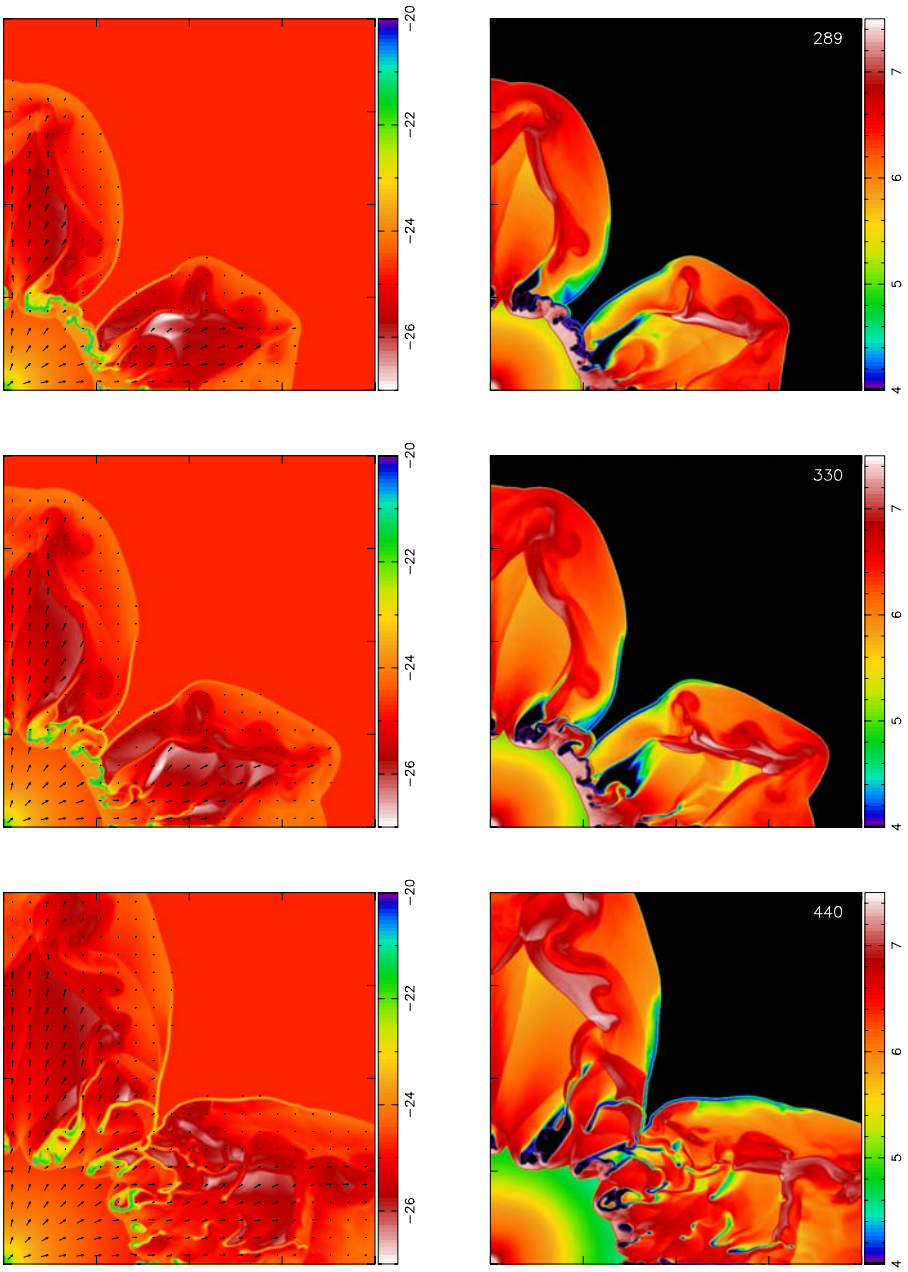

Fig. 7.— The time evolution. Case D, $n_c = 10^2$ cm^{-3}, $L_{SC} = 10^{41}$ erg s^{-1}. The same as Figure 5 at three different times: 2.9 $\times 10^5$ yr, 3.3 $\times 10^5$ yr and 4.4 $\times$ 10^5 yr, respectively. The panels show the full computational grid.

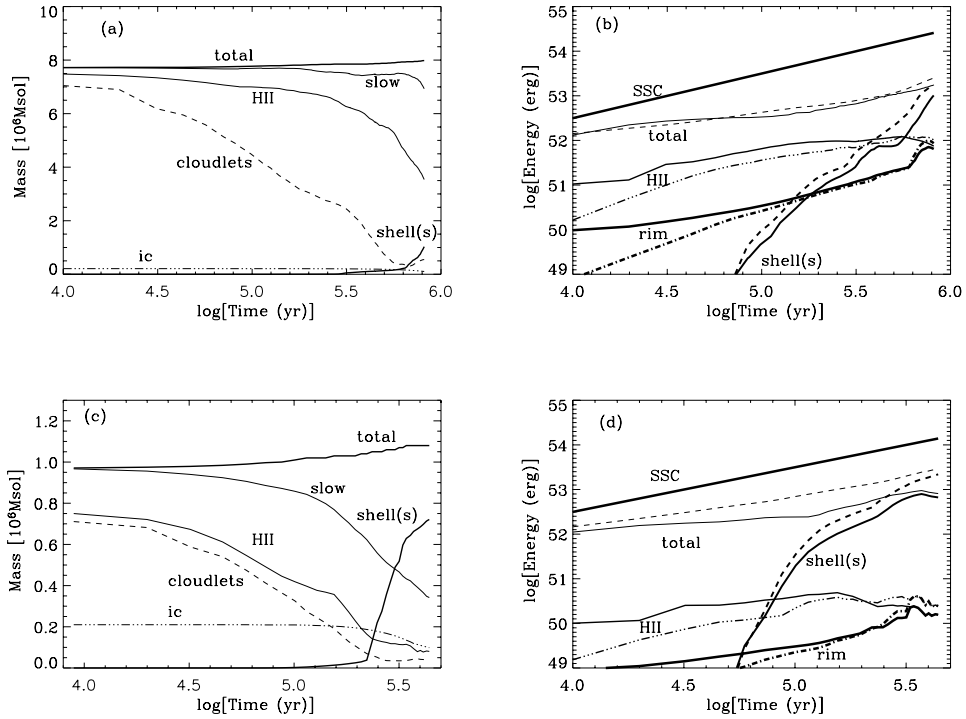

Fig. 8.— The time evolution. Mass and energy budget for the high density case C (upper panels) and the low density case D (lower panel). The various lines in figures a and c represent: Total mass within the computational grid, matter moving with less than 50 km s^{-1}, cloud (cloudlets) and intercloud (ic) matter that preserve their original density value, and HII and shells represent all the matter set into motion through a champagne flow and that has left the original cloudlet distribution volume, respectively. Panels b and d display the total amount of mechanical energy provided by the central cluster (SSC), the total kinetic (dashed line) and thermal (solid line) energy found within the computational grid. The other curves marked HII, rim and shells, display the kinetic (broken lines) and thermal (solid lines) energy stored in the ionized medium, or in the rim, or within the giant superbubbles.

function of time. The "HII" curve accounts for the photoionized gas set into motion through champagne flows. The final curve ("shells"), that appears towards the end of the calculations, accounts for all matter that has managed to stream out of the original cloudlet distribution. Figures 8b and d consider the energetics as a function of time of cases C and D, respectively. From top to bottom the various curves show: The total amount of kinetic energy delivered by the central star cluster (labelled "SSC"). The total amount of thermal (solid line) and kinetic energy (dashed line) within the computational grid (marked "total" in the figure). A comparison of the energy delivered by the central cluster with the addition of the latter two energies (total), shows that almost 90% of the SSC mechanical energy is radiated away throughout the evolution of case C, and 70% in case D. The remaining energy ends up being stored in the gas that has managed to stream out of the original cloudlet distribution (labelled "shells"). The other curves marked "HII", "rim" and "shells", indicate the thermal (solid lines) and kinetic energy (broken lines) stored in the ionized medium, part of which is in the photoionized outer rim, and finally the energy content within the large-scale expanding superbubbles, including the large-scale shells. Clearly, the latter amounts only to a small fraction of the energy delivered by the central SSC.

Figure 9 compares the size acquired by the various disturbances that develop in case C, within the flow. We have measured the location of the photoionized rim outer boundary, as well as the position of the ragged shell and of the reverse shock as a function of time. Also the dimensions of the large-scale superbubble that develops earlier in the calculation, measured from the point where energy is fed into it, at the edge of the channel carved through the cloudlet distribution (see Figure 9). The trend followed by the expanding photoionized rim is initially in excellent agreement with a champagne flow expansion speed of about 50 km s^{-1} (see Franco et al 1990), and is strongly decelerated (to 30 km s^{-1}) in the late part of the evolution as the giant superbubble wraps around it (see Figure 5). The trends followed by the other disturbances have been compared with the analytical formulation of a strong wind powered by a constant energy input rate and evolving into a constant density medium (see eg. Koo & McKee 1992). From the formulation of Koo & McKee we know that the reverse shock position is determined by: $R_{rs} = 0.77(L_{SC}/\rho_0)^{0.3} V_\infty^{-1/2} t^{0.4}$; where ρ_0 is the background density. As shown in Figure 9, an excellent agreement is reached if one assumes the full power of the wind (10^{41} erg s^{-1}) and a value of $\rho_0 = 100$ cm$^{-3} \times m_H$ instead of the cloudlet density ($n_c = 1000$ cm^{-3}), which we justify by the uneven density within the cloud stratum and particularly by the low density values assumed for the intercloud medium. Assuming the same value of ρ_0 for the leading shock, the expression $R_{ls} = 0.86(L_{SC}/\rho_0)^{0.2} t^{0.6}$, of Koo & McKee, leads to a disagreement of a factor of two with the location of the ragged shell. This is due to the increasingly larger loss of energy through the channels built through the cloud stratum, which enhance their width as the evolution proceeds. This increasingly larger loss

of energy is in fact fed into the large-scale superbubble and thus its leading shock instead of decelerating and causing a trend $R_{ls} \propto t^{0.6}$ (expected for a constant energy input rate) gives a trend $R_{ls} \propto t^{1.2}$, see Figure 9. This also implies that the energy input rate into the superbubble ($L_{SC} \propto t^{\alpha}$, grows as t^3, consistent with the shell energy budget in Figure 8b ($\alpha = log((E(t_2) - E(t_1))/E(t_1) + 1)/log(t_2/t_1) \approx 3.2$ if one considers the shell evolution between 10^5 yr and 3 $\times 10^5$ yr).

Further properties of the brightest filament or ragged shell may be derived from a consideration of the ram pressure exerted by the central wind ($\rho_w V_\infty^2$). From the wind mechanical energy ($\dot{E} = 1/2 \dot{M} V_\infty^2$) and the continuity equation that establishes that $\dot{M} = 4\pi R^2 \rho_w V_\infty$, one can derive an expression for $\rho_w = \dot{E}/(2\pi R^2 V_\infty^3)$ and thus the wind ram pressure $\rho_w V_\infty^2 = \dot{E}/(2\pi R^2 V_\infty)$. This is to be compared with the ragged shell ram pressure ($\rho_{rs} v_{rs}^2$) at different evolutionary times or considering different values of R. The expression is in good agreement with our calculations, leading to average number density values of the ragged shell of a few thousand particles per cm^3 at the start of the evolution (for an $R \sim 10$ pc) which fall to a several hundred particles cm^{-3} when the considered R is ~ 50 pc.

The above estimate can be directly applied to well known sources. Such is the case of the brightest shell in NGC 604, for which the average distance to the exciting cluster is 30 pc (González Delgado & Pérez 2000) and the inferred expansion speed amounts to 35 km s^{-1} (cf. figures 3 and 4 in Tenorio-Tagle et al. 2000), leading to an average density of $\lessapprox 100$ cm^{-3} (the exact value depending on the luminosity of the best fitted model, cf. table 4 in González Delgado & Pérez 2000) in agreement with the data (cf. figure 10 of Maíz Apellániz et al. 2004). The agreement however leads also to a controversy. The dynamical time for such a shell ($t_{dyn} \sim 10^6$ yr) is smaller than the life time estimated ($\sim 3 \times 10^6$ yr) for the exciting stars (González Delgado & Pérez 2000). Possible solutions of such a puzzle are: a) Clusters born in low metallicity galaxies are to undergo much milder winds before the supernova era starts (~ 3 Myr; see Leitherer & Heckman 1995), allowing for a better match between the dynamical time and the stellar lifetime. b) Also, a dense cocoon around the newly sources may delay the impact of winds and photoionization in the background media, bringing into a better agreement between the two times here cosidered. Once the full energy from sequential supernovae and the displacement of the dense cocoon surrounding the newly formed cluster are overcome, the giant structure of HII regions and HII galaxies would develop within a few 10^6 yr while the giant shells acquire kpc dimensions and the ragged shell is displaced to a few tens of pc away from the central source. At the same time that the production of UV radiation would steadely drop making less easy the detection of the nebular structure at optical wavelengths.

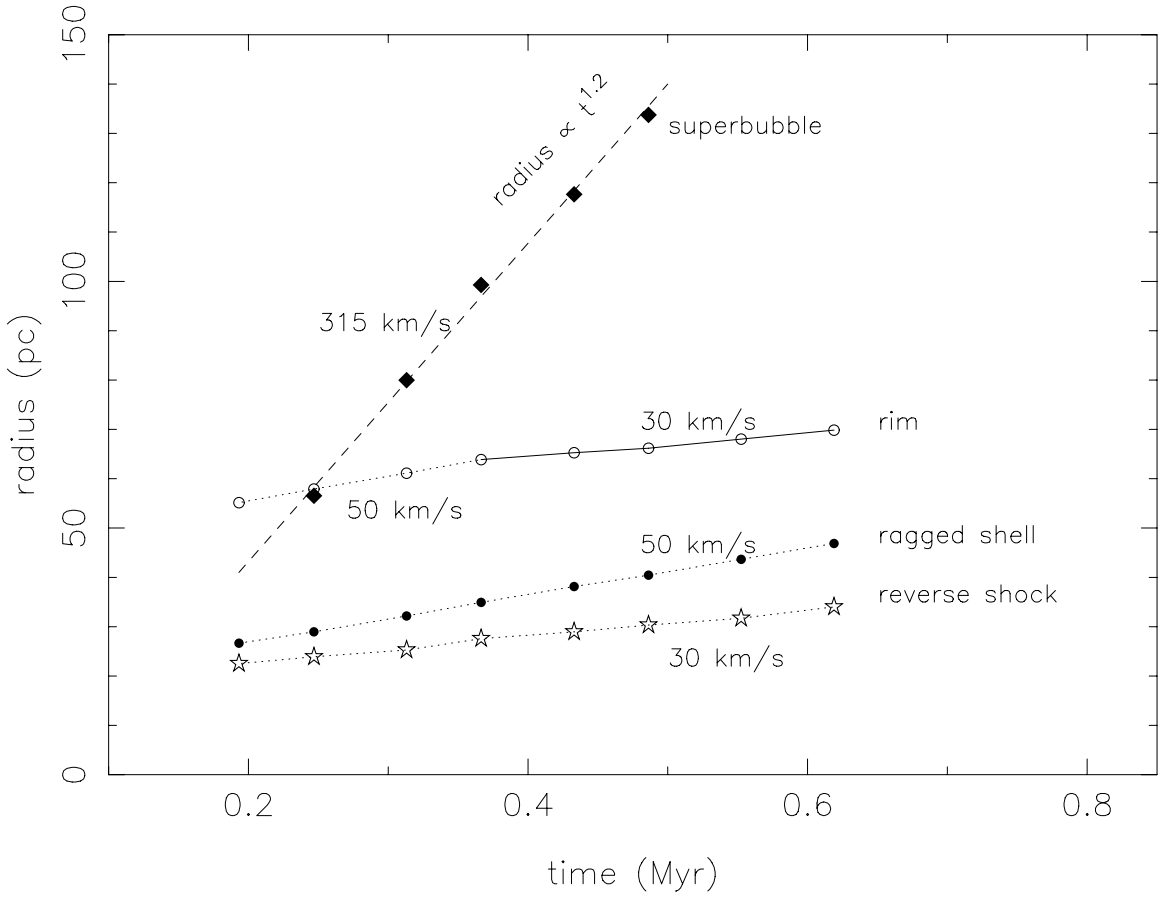

Fig. 9.— The time evolution. The location of the various fronts that develop within the flow for case C, as a function of time. The figure indicates the location of the champagne rim outer edge, the ragged shell, the reverse shock and the furthest edge of the giant superbubble. All of them with an indication of their expansion speed. The radius of the giant bubble has been fitted with a power law in which $r \propto t^{1.2}$.

3. Discussion

We have shown here the effects of feedback from a massive stellar cluster into a selected cloudlet distribution, which although arbitrary, as it could have had a different extent or it could have considered clouds of different sizes, separations and locations, it has allowed us to explore a wide range of possibilities. These however, have lead to the two main possible physical solutions to be expected: partial pressure confinement of the shocked wind, and a stable and long-lasting filtering of the thermalized wind through the cloudlet stratum. Similar solutions would have been found for different cloud densities and cloud distributions and/or for different SSC masses (M_{SC}) or energetics. Thus despite the arbitrary and simple boundary and initial conditions here assumed, the structures that develop within the flow resemble the structure of giant HII regions and HII galaxies (see Figure 10). In particular we refer to the giant and multiple well structured shells evident at optical wavelengths, often referred to as nested shells (see Chu & Kenniccutt 1994), that enclose a hot X-ray emitting gas, as in 30 Dor (Wang 1999) and NGC 604 (Maíz-Apellániz et al. 2004). The calculations also lead to the slowly expanding brightest filament (or ragged shell) present in all sources close and around the exciting stars, and to the elongated, although much fainter, filaments on either side of the open channels that reseamble the ends of elongated columns into the giant superbubbles.

None of these structural features appear in calculations that assume a constant density ISM, nor in those that allow for a constant density molecular cloud as birth place of the exciting sources, or in calculations where the sources are embedded in a plane stratified background atmosphere. For all of these features to appear, a clumpy circumstellar medium seems to be a necessary requirement. A medium that would refrain the wind from an immediate exit into the surrounding gas and that would also allow for the build up of multiple channels through which the wind energy would flow in a less unimpedded manner. And thus giant HII regions and HII galaxies, both powered by massive star formation events producing an ample supply of UV photons and a powerful wind mechanical energy, all of them seem to process their energy into a stratum of dense cloudlets sitting in the immediate vicinity of the star formation event.

Our calculations confirm many of the results by Pittard et al. (2005) for the rapid sequence of the hydrodynamical events that emerge from the wind-cloud early interaction. In particular, a global bow shock is to engulf two or more cloudlets if the separation between them is smaller than their diameter while individual bow shocks are set around each condensation when they are further appart from each other, as shown in all small-scale Figures 2, 4 and 6. Also, the elongated tails of ablated matter behind bow shocks, are not necessarily aligned with the incoming stream velocity vector. The deviation in the alignment of tails

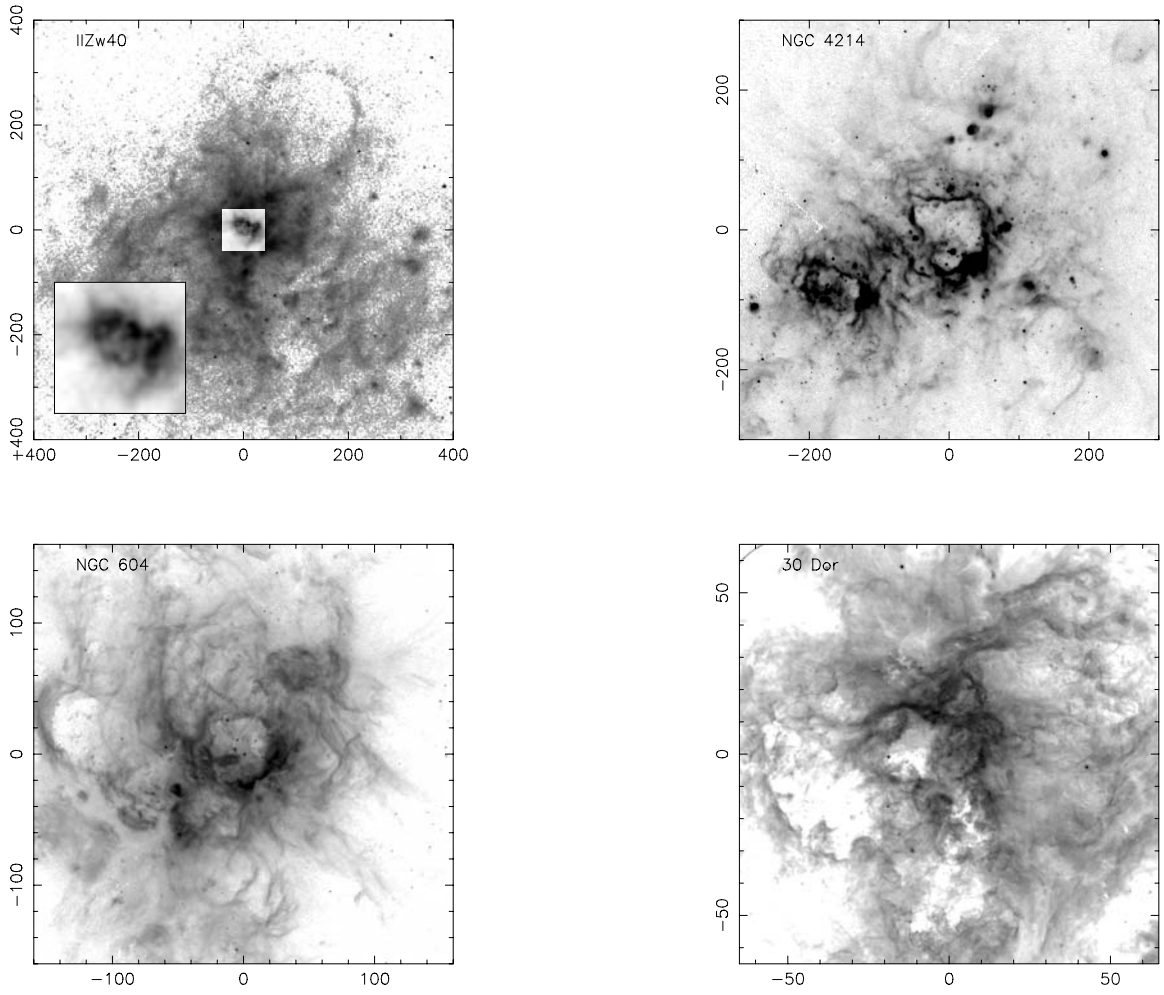

Fig. 10.— The observational evidence. HST Hα images of the IIZw 40, the central regions of NGC 4214, and NGC 604 (in M33), and an ESO NTT image of 30 Doradus, all of them ploted in a linear parsec scale. For IIZw 40 the inset shows the most central region. HST images were retrieved from the HST archive at STScI. The NTT image courtesy of Jesús Maíz-Apellániz and Rodolfo Barbá.

is due to pressure gradients on either side of each cloud. As shown also by Pittard et al. (2005) and in our small-scale figures, tails that show deviations from the alignment with the incoming wind end up pointing away from the cloudlets, and when the flow is subsonic the tails end up pointing towards each other. Here we have shown that the ablated matter that composes the various tails, ends up merging with other cloudlets further downstream to eventually compose the almost even density, slow moving ragged shell.

Given the large number of possibilities regarding SSCs, we consider that cases A and B also seem relevant. One can imagine situations in which the stellar photon output is more developed and dominant than the winds, as in the initial stages of the evolution of coeval clusters, and thus leading to results similar to those of case B. Also cases in which the photon flux has dropped sufficiently, as predicted for coeval clusters after 3 Myr of evolution, leading (as in case A) to a long-lasting SSC wind as the dominant feedback mechanism.

In the calculations here shown, as the selected cloudlet stratum covers most of the sky above the central SSC, all calculated cases follow a similar evolutionary track in which two competing hydrodynamical processes define the time evolution. On the one hand, photoionization that aims at establishing a constant density medium everywhere and, on the other, the wind mechanical energy that looks for all possible exits out of the cloudlet distribution. In all cases that consider both effects, the ensemble of clouds ends up being driven to compose an almost constant density, low velocity ragged shell, that acts as a barrier to most of the shocked wind. In this way the wind matter becomes subsonic upon crossing the reverse shock and trapped behind the ragged shell. On the other hand, channels through the cloudlet stratum allow for the rapid streaming of the shocked wind gas and lead to the build up of large-scale superbubbles with a pronounced inner filamentary structure. The latter is promoted by the ablation of clouds from each of the channels inner edges. The calculations also show that for individual giant bubbles to be easily recognized they would have to be fed through channels in the cloud stratum, carved well further apart from each other. Neighboring channels would rapidly end up bursting their carried shocked wind energy into a single shell.

Photoionization tends to equalize the density everywhere, causing an evolution towards a higher even pressure, however its power to slow the effects of the wind, its power to make the wind less dominant strongly depend on the initial contrast density between the cloud and intercloud medium. And thus, the larger the initial contrast density, the less dominant and longer lasting the impact of the wind would be.

We are grateful to an anonymous referee for useful suggestions that have led to an improvement of this work.

GTT acknowledges finantial support from the Secretaría de Estado de Universidades e Investigación (España) through grant SAB2004-0189 and the hospitality of the Instituto de Astrofísica de Andalucía (IAA, CSIC) in Granada, Spain. This study has been partly supported by grants AYA2004-08260-C03-01 and AYA 2004-02703 from the Spanish Ministerio de Educación y Ciencia, grant TIC-114 from Junta de Andalucía and Conacyt (México) grant 47534-F.

This research has made use of NASA's Astrophysics Data System Bibliographic Services. Some of the data presented in this paper were obtained from the Multimission Archive at the Space Telescope Science Institute (MAST). STScI is operated by the Association of Universities for Research in Astronomy, Inc., under NASA contract NAS5-26555. Support for MAST for non-HST data is provided by the NASA Office of Space Science via grant NAG5-7584 and by other grants and contracts. We have made use of STSDAS and PyRAF which are products of the Space Telescope Science Institute, which is operated by AURA for NASA. IRAF is distributed by the National Optical Astronomy Observatories, which are operated by the Association of Universities for Research in Astronomy, Inc., under cooperative agreement with the National Science Foundation.

REFERENCES

Cairós, L. M., Caon, N., Vílchez, J. M., González-Pérez, J. N., Muñoz-Tuñón, C., 2001, ApJS, 136, 393

Chevalier, R. A. & Clegg, A. W., 1985, Nature, 317, 44

Chu, Y.H. & Kennicutt, R., 1994, ApJ, 425, 720

Comeron, F. 1997, A&A 326, 1195

Franco, J., Shore, S. & Tenorio-Tagle, G., 1994, ApJ 436,795

Franco, J., Tenorio-Tagle, G. Bodenheimer, P., 1990, ApJ 349, 126

Garcıa-Segura, G. & Franco, J., 2004, RMxAC 22,131

González Delgado, R. M. & Pérez, E., 2000, MNRAS 317, 64

Grimes, J. P., Heckman, T., Strickland, D., 2005, ApJ, 628, 187

Ho, L. C., 1997, Rev.Mex.AA, Conf. Ser. 6, 5

Hosokawa, T. & Inutsuka, S., 2005 astro-ph/0511165

Klein, R., McKee, C. & Colella, P., 1994, ApJ 420 213

Koo, B.; & McKee, C. F., 1992, ApJ, 388, 93

Lamers, H., et al., 2004, in ASP Conf. Ser. 322, The formation and evolution of massive young star clusters, eds. H. J. G. L. M. Lamers, L. J. Smith & A. Nota (San Francisco: ASP)

Larson, R., 1988, in Galactic and Extra Galactic Star Formation. ed. R. E. Pudritz & J. M. Fich (Dordrecht: Kluwer), 459

Leitherer, C. & Heckman, T. M., 1995, ApJS, 96, 9

Mac Low, M.-M. & Klessen, R. S., 2004, Rev. Mod. Phys. 76, N1, 125

Maíz-Apellániz, J., Pérez, E., Mas-Hesse, J. M., 2004, AJ, 128, 1196

Maíz-Apellániz, J., Muñoz-Tuñón, C., Tenorio-Tagle, G., Mas-Hesse, J. M., 1999, A&A, 343, 64

Martin, C. L., Kobulnicky, H. A., Heckman, T. M., 2002, ApJ, 574, 663

Melnick, J., Tenorio-Tagle, G., Terlevich, R., 1999, MNRAS, 302, 677

Melo, V. P., Muñoz-Tuñón, C., Maíz-Apellániz, J., Tenorio-Tagle, G., 2005, ApJ, 619, 270

Muñoz-Tuñón, C., Tenorio-Tagle, G., Castaneda, H. O. Terlevich, R., 1996, AJ 112, 1636

Pasquali, A., Gallagher, J. S. & de Grijs, R., 2004, A&A 415, 103

Pittard, J. M., Dyson, J. E., Falle, S. A. E. G.& Harquist, T. W., 2005, MNRAS (in press)

Raga, A. C., Velázquez, P. F., Cantó, J, Masciadri, E. & Rodrı´guez, L. F., 2001, ApJ 559, L33

Raymond, J. C., Cox, D. & Smith B. W., 1976, ApJ 204, 290

Sabalisck, N. S. P., Tenorio-Tagle, G., Castaneda, H. O., Muñoz-Tuñón, C., 1995, ApJ, 444, 200

Silich, S., Tenorio-Tagle, G. & Rodríguez González, A. 2004, ApJ, 610, 226

Telles, E., Muñoz Tuñón, C. & Tenorio-Tagle, G., 2001, ApJ. , 548, 671

Tenorio-Tagle, G., 1979, A&A, 71, 59

Tenorio-Tagle, G. & Bodenheimer, P., 1988, ARA&A, 26, 145

Tenorio-Tagle, G. & Muñoz-Tuñón, C., 1997, ApJ, 478, 134

Tenorio-Tagle, G. & Muñoz-Tuñón, C., 1998, MNRAS, 293, 299

Tenorio-Tagle, G. & Muñoz-Tuñón, C., Pérez, E., Maíz-Apellániz, J., & Medina-Tanco, G., 2000, ApJ, 541, 720

Tenorio-Tagle, G. Silich, S. & Muñoz-Tuñón, C., 2005, in ASP Conf. Ser., Resolved Stellar Populations, ed. D. Vals-Gabaud & M. Chavez (in press)

Tenorio-Tagle, G. & Rozyczka, M., 1986, A&A 155, 120

Wang, Q. D., 1999, ApJ, 510, L139

Yang, H., Chu, Y., Skillman, E. D., Terlevich, R., 1996, AJ, 112, 146

Yorke, H. W., Tenorio-Tagle, G., Bodenheimer, P. & Rozyczka, M., 1989, A&A 216, 207

This preprint was prepared with the AAS LaTeX macros v5.0.